The Astrophysical Journal, 837:182 (9pp), 2017 March 10 https://doi.org/10.3847/1538-4357/aa5da4

ALMACAL II: Extreme Star Formation Rate Densities in Dusty Starbursts Revealed by ALMA 20 mas Resolution Imaging

I. Oteo[1,2], M. A. Zwaan[2], R. J. Ivison[1,2], I. Smail[3,4], and A. D. Biggs[2]
[1] Institute for Astronomy, University of Edinburgh, Royal Observatory, Blackford Hill, Edinburgh EH9 3HJ, UK; ivanoteogomez@gmail.com
[2] European Southern Observatory, Karl-Schwarzschild-Str. 2, D-85748 Garching, Germany
[3] Centre for Extragalactic Astronomy, Department of Physics, Durham University, South Road, Durham DH1 3LE, UK
[4] Institute for Computational Cosmology, Department of Physics, Durham University, South Road, Durham DH1 3LE, UK
Received 2016 July 20; revised 2017 January 19; accepted 2017 January 30; published 2017 March 16

Abstract

We present ultrahigh spatial resolution (∼20 mas or 150 pc) ALMA observations of the dust continuum at 920 μm and 1.2 mm in two submillimeter sources at $z = 3.442$, ALMACAL–1 (A–1: $S_{870\,\mu m} = 6.5 \pm 0.2$ mJy) and ALMACAL–2 (A–2: $S_{870\,\mu m} = 4.4 \pm 0.2$ mJy). About half of the star formation in each of these sources is dominated by a single compact clump (FWHM size of ∼350 pc). In A–1, two additional fainter clumps are found. The star formation rate (SFR) surface densities of all these clumps are extremely high, $\Sigma_{SFR} \sim 1200$ to $\sim 3000\ M_{\odot}\ yr^{-1}\,kpc^{-2}$, the highest rates found in high-redshift galaxies. Given their geometry and identical redshifts, there is a possibility that A–1 and A–2 are the lensed images of a single background source that are gravitationally amplified by the blazar host. If this were the case, the effective radius of the dusty galaxy in the source plane would be $R_{eff} \sim 40$ pc and the demagnified SFR surface density would be $\Sigma_{SFR} \sim 10{,}000\ M_{\odot}\ yr^{-1}\,kpc^{-2}$, comparable with the eastern nucleus of Arp 220. Although we cannot rule out an AGN contribution, our results suggest that a significant percentage of the enormous far-IR luminosity in some dusty starbursts is extremely compact. The high Σ_{SFR} in these sources could only be measured thanks to the ultrahigh-resolution ALMA observations used in this work, demonstrating that long-baseline observations are essential to study and interpret the properties of dusty starbursts in the early Universe.

Key words: dust, extinction – galaxies: high-redshift – infrared: galaxies – ISM: molecules – submillimeter: galaxies – submillimeter: general

1. Introduction

Two decades ago, the first large format bolometer cameras on single-dish submillimeter telescopes discovered a population of galaxies that were forming stars at tremendous rates, the so-called submillimeter galaxies (SMGs, Smail et al. 1997; Barger et al. 1998; Hughes et al. 1998; Blain et al. 2002). Later, it was reported that these starbursts were observed predominantly at high redshift, $z \sim 1 - 3$ (Chapman et al. 2005; Simpson et al. 2014). One of the main problems of these single-dish submillimeter observations is their large beams, typically $>10''$. This complicates the multiwavelength counterpart identification in the absence of higher resolution (sub) millimeter follow-up and prevents us from studying the morphology of dust emission, which is needed to help interpret the properties of the interstellar medium (ISM) in dusty starbursts.

Interferometric observations at arcsecond and subarcsecond resolution revealed that most SMGs are major mergers, based on morphological and kinematics arguments (e.g., Tacconi et al. 2008; Engel et al. 2010). Building on early indications from radio and submillimeter imaging (Ivison et al. 2007; Wang et al. 2011), ALMA revealed that single-dish submillimeter sources are sometimes resolved into several distinct components (Hodge et al. 2013; Karim et al. 2013), although this is not always the case (Barger et al. 2014), and it is not clear that all subcomponents are at the same redshift and are therefore physically associated. Based on limited ALMA data, Ikarashi et al. (2015) reported that the dust in SMGs at $z > 3$ is confined to a relatively compact region, with a FWHM size of $\sim 0\farcs2$ or ∼1.5 kpc. This average value is compatible with the size of SMGs at slightly lower redshifts reported in Simpson et al. (2015). Owing to the still modest spatial resolution in these works, it was not possible to explore any subgalactic structure within the SMGs. Using observations at higher spatial resolution ($\sim 0\farcs1$), Oteo et al. (2016a) studied the morphology of two interacting starbursts at $z \sim 4.4$. The small beam size resolved the internal structure of the two sources and revealed that the dust emission is smoothly distributed on ∼kiloparsec scales, in contrast with the more irregular [C II] emission.

Analyzing strongly lensed sources offers an alternative to high spatial resolution observations (Negrello et al. 2010; Swinbank et al. 2010; Bussmann et al. 2013, 2015). Arguably, the best example is the ALMA study for SDP.81 (ALMA Partnership et al. 2015), a strongly lensed starburst at $z \sim 3$ (Frayer et al. 2011; Dye et al. 2014; Negrello et al. 2014) selected from the *Herschel*-ATLAS (Eales et al. 2010). Dye et al. (2015) modeled the lensed dust and CO emission of SDP.81 (see also Rybak et al. 2015a, 2015b), and the dynamical analysis presented in Swinbank et al. (2015) revealed that SDP.81 comprises at least five star-forming clumps, which are rotating with a disk-like velocity field. However, with lensed galaxies, the results (especially those lensed by galaxy-scale potential wells) must rely on accurate lens modeling that ensures that all the recovered source-plane emission is real and not an artifact of the modeling itself. Furthermore, and importantly, even relatively bright intrinsic emission can lie below the detection threshold if the geometry is not favorable, which results in a misleading picture.

Thanks to the unique sensitivity and long-baseline capabilities of ALMA, ultrahigh spatial resolution observations can be carried out for the first time in unlensed far-infrared

(FIR)-bright sources. In this work we present ultrahigh spatial resolution observations (∼20 mas) of a pair of submillimeter sources at $z = 3.442$ selected from ALMACAL (Oteo et al. 2016b). The main difference between this and previous work (Ikarashi et al. 2015; Simpson et al. 2015) is that we use a significant number of very long baselines, providing ∼10× better spatial resolution. Furthermore, our in-field calibrator and subsequent self-calibration ensures near-perfect phase stability on the longest baselines. Additionally, we have two independent data sets in ALMA band 6 (B6) and band 7 (B7), which prove the reliability of the structure we see.

The paper is structured as follows: Section 2 presents the data set used in this work. Section 3 presents the redshift confirmation of our two sources and their FIR spectral energy distribution (SED). In Section 4, we discuss the morphology of the dust emission in our sources at 0.″02 or ∼150 pc resolution. Finally, Section 5 summarizes the main conclusions of the paper. A Salpeter (1955) initial mass function (IMF) is assumed to derive star formation rates (SFRs). We assume a flat universe with $(\Omega_m, \Omega_\Lambda, h_0) = (0.3, 0.7, 0.7)$. For this cosmology, the angular scale is ∼7.3 kpc per arcsecond at $z = 3.442$, the redshift of the sources under study.

2. Data Set: ALMACAL

Using ALMA calibration data, we are carrying out a wide and deep (sub)millimeter survey, ALMACAL. The strategy of the survey and the details of data calibration and source extraction can be found in Oteo et al. (2016b). Briefly, our survey takes advantages of the huge amount of ALMA calibration data that are routinely acquired during the execution of ALMA science projects. By combining compatible data for different calibrators, it is possible to cover areas large enough and r.m.s. levels low enough to enable the detection of faint SMGs.

At the present stage of the survey, we are reaching noise levels down to ∼15 μJy beam^{-1} at subarcsecond resolution in more than 350 calibrator fields, representing an area of more than 20 sq arcmin (I. Oteo et al. 2017, in preparation). We focus this paper on the two submillimeter sources found around the calibrator J1058+0133: ALMACAL–1 (A–1) and ALMACAL–2 (A–2), see Figure 1, which are the brightest submillimeter sources found so far in ALMACAL.

The ALMACAL data used in this work can be classified into two different groups according to the spatial resolution they provide. On one hand, we use medium spatial resolution data (beam sizes typically larger than 0.″3) that are part of the automated ALMACAL data extraction and calibration and are used to measure the unresolved dust continuum emission in our two submillimeter sources to search for emission lines to confirm their redshift (see Section 3). Because of their compact nature, A–1 and A–2 remain unresolved in the medium-resolution data.

In addition, and with the aim of studying the morphology of the dust emission in our two submillimeter sources (Section 4), we also use ultrahigh spatial resolution data especially extracted from the ALMA archive for the analysis presented in this work. Since no bright emission lines are covered by the spectral setup of the ultrahigh spatial resolution observations, we focus on the continuum dust emission. There are ultrahigh spatial resolution observations in B3, B6, and B7. No continuum emission is detected in B3 because we lack the necessary depth. We therefore focus our analysis on B6 and B7.

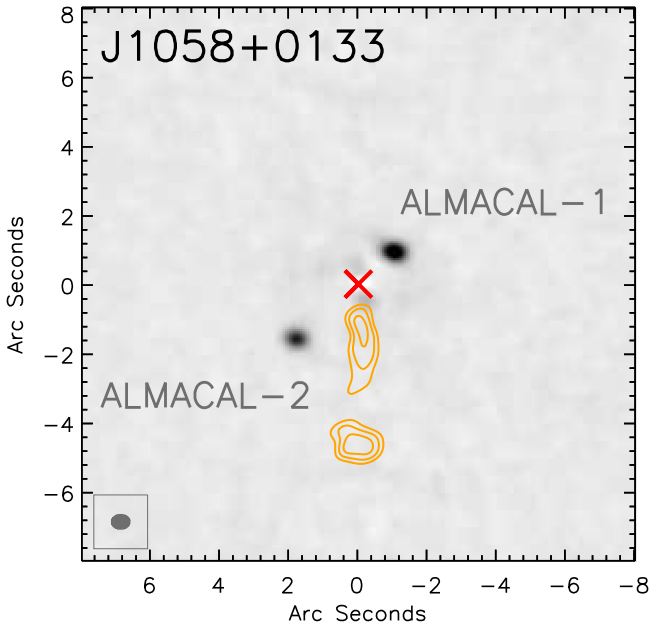

Figure 1. Continuum map (870 μm) of the two luminous submillimeter sources at $z = 3.442$ (ALMACAL–1 and ALMACAL–2) discovered around the calibrator J1058+0133 at $z = 0.88$. The coordinates of the two sources can be found in Table 1. The calibrator has been subtracted from the data in the *uv* plane by using a point-source model and is located at the position marked by the red cross. Orange contours represent the jet emanating from J1058+0133, revealed by 3 mm imaging. The image is 16″ on each side, and the beam of the 870 μm continuum observations is shown on the bottom left. It should be pointed out that given the observed geometry and similar redshifts, there is a possibility that ALMACAL–1 and ALMACAL–2 are the lensed images of a single background source that is being gravitationally amplified by the blazar host (see Section 4.1).

The extraction and calibration of the ultrahigh-resolution data is done in exactly the same way as for the medium-resolution data, including self-calibration to improve image quality. Using Briggs weighting with a `robust` parameter equal to 0.5, we obtain a beam size of 25 mas × 18 mas at ∼920 μm (B7), meaning a spatial resolution of 180 pc × 130 pc at the redshift of the two sources. The continuum sensitivity is $\sigma_{B7} = 30$ μJy beam^{-1}. The spatial resolution of the B6 observations is 29 mas × 25 mas, with an rms level of $\sigma_{B6} = 50$ μJy beam^{-1}. The spatial resolution provided by these observations is about 10× times better than those reported so far in any previous unlensed high-redshift starburst, and it is close to the typical size of giant molecular clouds (∼50 pc).

3. A Pair of Submillimeter Sources at $z = 3.442$

As pointed out in Oteo et al. (2016b), one of the key advantages of using ALMA calibrators to study the submillimeter galaxy population is that they are typically observed in multiple ALMA bands. This allows us to (1) have a good sampling of the FIR SED of the detected galaxies; (2) find redshifts by carrying out blind searches of (sub)millimeter emission lines (including CO, H_2O, [C I], [C II], etc.). The two submillimeter sources found around calibrator J1058+0133 perfectly exemplify these two points. They were initially discovered in B6 and B7 as two bright sources near J1058+0133, which is a bright blazar at $z \sim 0.88$ used routinely as

an ALMA calibrator (Oteo et al. 2016b). We initially thought that they were part of a jet emanating from the calibrator. However, ALMA B3 data revealed that J1058+0133 does have a strong jet, but not in the direction from the calibrator to either of the two submillimeter sources (see Figure 1). The flux density ratio between 870 μm and 1.2 mm of each source (in addition to the lack of continuum detection in B3 and B4) was compatible with them being high-redshift sources, although it could still be compatible with the two sources being companions of the bright calibrator, located at its redshift.

We then searched for emission lines from the two sources assuming that they were at the same redshift of the calibrator, but found nothing. However, a blind search for emission lines in their (sub)millimeter spectrum revealed two emission lines in each component, unambiguously confirming a redshift of $z \sim 3.442$. Further data for this calibrator was then extracted from the ALMA archive, and up to nine potential emission lines were identified in each component, as shown in Figure 2. We have detected ^{12}CO(14–13), ^{12}CO(13–12), ^{12}CO(11–10), ^{12}CO(10–9), ^{12}CO(9–8), ^{12}CO(6–5), $H_2O(3_{12}–3_{03})$, and weak $H_2O(4_{22}–4_{13})$ and $H_2O(2_{02}–1_{11})$ transitions in one or both sources. The median line width of the lines in A–1 and A–2 are 520 and 417 km s^{-1}, respectively, and there is evidence that our measured water lines are slightly wider than the CO transitions; this will be reassessed as more data for J1058+0133 become available. For a given source, the velocity shifts can be as large as $\sim$100 km s^{-1}. These are lower than those found in other bright starbursts such as SGP38326 (Oteo et al. 2016a) or HATLAS J084933 (Ivison et al. 2013).

The CO spectral line energy distribution (SLED) of A–1 and A–2, including data for lower-J transitions from other facilities where J1058+0133 has also been used as a calibrator (for example the JVLA), will be presented in a subsequent paper. However, it is important to point out here that A–1 is warmer (see Section 3.1 and Table 1), has relatively bright ^{12}CO (13–12), ^{12}CO(14–13), and $H_2O(4_{22}–4_{13})$ lines, and its CO SLED seems to plateau at $J = 10 - 13$, suggesting an influential AGN in A–1 and less so in A–2, for which the upper limits in the high-J CO lines suggest a less excited CO SLED. Despite the possible influence of an AGN on the molecular line properties, with the data at hand, we cannot estimate the contribution of the possible AGN to the total IR luminosity of the source.

The redshift of A–1 and A–2 (see Table 1) clearly indicates that they are not related to the calibrator (at $z \sim 0.88$). It might be argued that the two submillimeter sources are lensed components of the same background galaxy, as is suggested by the apparent symmetry of the two sources with respect to the calibrator. However, despite the high signal-to-noise ratio (S/N) of the multiband continuum detections, there is no sign of an Einstein ring or extended emission connecting the two sources, as is sometimes seen in the lensed dust emission of high-redshift SMGs (see for example Bussmann et al. 2013, 2015; ALMA Partnership et al. 2015; Dye et al. 2015). Moreover, ^{12}CO(13–12) and ^{12}CO(14–13) are not detected in A–2, although the low rms of the spectra would have allowed detections if the CO SLEDs of A–1 and A–2 were the same, as expected if they A–1 and A–2 were lensed components of the same background source. Furthermore, the FIR SED of the two sources are different (see Section 3.1), and this is not compatible with them being lensed by the blazar host galaxy. Despite the arguments supporting the idea that A–1 and A–2 are not lensed, we explore the consequences of possible lensing in the conclusions of this paper in Section 4.1.

If they are two SMGs, then A–1 and A–2 are separated by 28 kpc in projection, suggesting tidal interaction may have triggered star formation in both systems. If observed with a single-dish submillimeter telescope, our two submillimeter sources would have appeared in the image as a single unresolved blob. The separation between A–1 and A–2 is about twice times the projected separation between the two interacting components of SGP38326 at $z = 4.425$ (Oteo et al. 2016a) and comparable to the separation between merging the HyLIRGs at $z \sim 2.4$ in Ivison et al. (2013). The 3.″8 separation is compatible with the distance between the multiple components that SMGs are normally resolved into, as revealed by high-resolution radio or ALMA observations (Ivison et al. 2007; Hodge et al. 2013; Karim et al. 2013; Simpson et al. 2015).

3.1. The Far-IR SEDs

In order to determine the dust temperature of A–1 and A–2, we have fitted their FIR SED (using all available photometry in B6, B7, B8, and B9) with optically thin models, where the optical depth is small (Casey 2012). The results are presented in Figure 3. Uniquely, we have performed FIR SED fits with subarcsecond-resolution photometry, unlike all previous work on high-redshift SMGs, where the large beams of the single-dish observations prevent accurate deblending of the multiple components that SMGs are typically resolved into (Hodge et al. 2013; Karim et al. 2013; Simpson et al. 2015). It should be noted that we assume here that the total IR luminosity is due to star formation rather than AGN activity.

Since observations are available in almost all frequencies covering B6 and B7, we have split the observations in each band into two subbands corresponding to the two halves of each band. In this way, we have six photometric points in total (see values in Table 1), and a finer coverage of the FIR SED. Table 1 quotes the dust temperature derived for A–1 and A–2 by assuming a dust emissivity of $\beta = 2.0$, which is the average value found for similarly bright SMGs (Magnelli et al. 2012). It should be noted that lower β values would give higher dust temperatures (for example, A–1 would have $T_D = 48.0 \pm 1.4$ K for $\beta = 1.5$). However, the χ^2 of the fits would not be significantly different, and additional photometric information is required to distinguish between different values of β. The observed FIR SEDs suggests that A–1 is warmer than A–2.

In order to derive the total IR luminosity of each source (see Table 1), we have fitted their FIR SEDs using optically thin models (Casey 2012) with a dust emissivity of $\beta = 2.0$ (i.e., compatible with the dust temperature determination), including a mid-IR power law with a slope of $\alpha = 2.25$, which is a good representation of the mid-IR of dusty sources (Casey 2012). The assumed mid-IR power law provides a mid-IR SED similar to the one found for the average SMG population (Swinbank et al. 2014). The SFR of A–1 and A–2 has then been derived from the total IR luminosity assuming the classical Kennicutt (1998) calibration and a Salpeter IMF (see Table 1). As expected from their brightness, the SFR of our two submillimeter sources is very high, revealing extreme star formation and placing A–1 and A–2 among the most luminous starbursts at $z \sim 3$–4. The T_D and L_{IR} (see Table 1) of A–1 and A–2 are compatible to those found for the classical population of single-dish submillimeter-detected SMGs (Simpson et al.

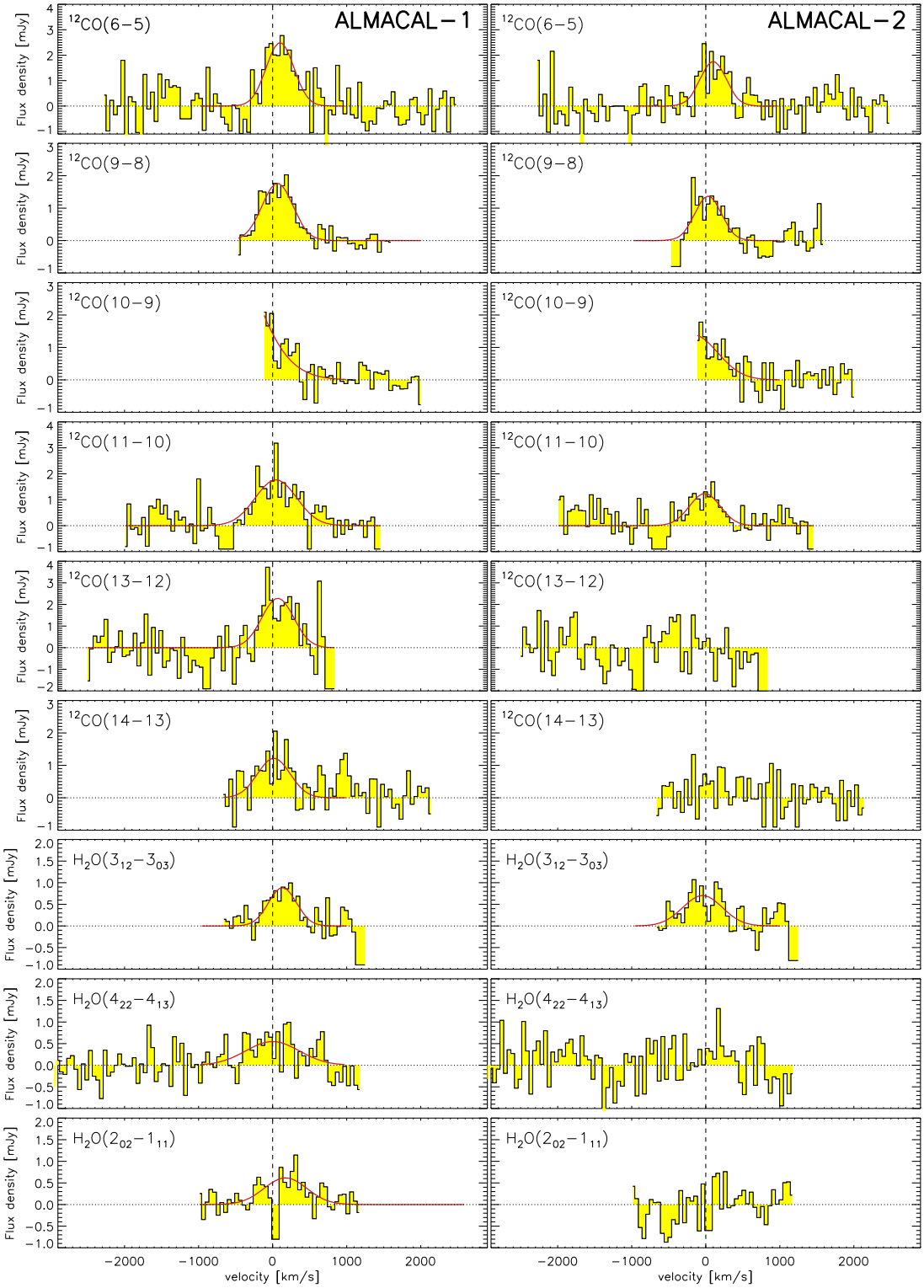

Figure 2. Continuum-substracted spectra showing the coverage of emission lines in our two submillimeter sources, ALMACAL–1 (left) and ALMACAL–2 (right). Up to nine emission lines are detected in each source, unambiguously confirming that their redshift is $z = 3.442$. The detected emission lines (except ^{12}CO(10–9), which is only half covered) are fit with Gaussian profiles (plotted as the red curves) in order to calculate their observed fluxes. The absence of a Gaussian fit in a given panel means that the corresponding line has not been detected. The vertical dashed lines indicate $v = 0$ km s^{-1} for a redshift $z = 3.442$. It should be pointed out that the redshift confirmation has been obtained from high-J CO and H_2O lines, which is unusual for FIR-bright sources, where redshift confirmation is normally achieved using spectral scans in the 3 mm band (Weiß et al. 2009, 2013; Asboth et al. 2016; Oteo et al. 2016a; Strandet et al. 2016).

2014; Swinbank et al. 2014), and they would have been selected individually as SMGs if they had been located in cosmological fields where FIR/(sub)millimeter surveys have been carried out.

Figure 3 compares the FIR SED of A–1 and A–2 with FIR SEDs for the average population of SMGs in the ALESS survey (Swinbank et al. 2014) and Arp 220. These two templates have been shifted to $z = 3.442$ and scaled to the

Table 1
Observed Properties of the two SMGs Detected around Calibrator J1058+0133

	A–1	A–2
R.A.	10:58:29.7	10:58:29.5
Decl.	+01:33:57.2	+01:33:59.7
z	3.4433 ± 0.0005	3.4431 ± 0.0005
$S_{460\,\mu m}$ [mJy]	23.3 ± 1.3	12.8 ± 0.8
$S_{750\,\mu m}$ [mJy]	10.5 ± 0.6	6.9 ± 0.3
$S_{870\,\mu m}$ [mJy]	6.5 ± 0.2	4.4 ± 0.2
$S_{1000\,\mu m}$ [mJy]	3.8 ± 0.2	2.7 ± 0.2
$S_{1225\,\mu m}$ [mJy]	2.0 ± 0.1	1.5 ± 0.1
$S_{1350\,\mu m}$ [mJy]	1.8 ± 0.2	0.9 ± 0.1
T_{dust} [K] ($\beta = 2.0$)	39 ± 2	35 ± 1
$\log(L_{IR}/L_{\odot})$	12.7 ± 0.1	12.5 ± 0.1
SFR [$M_{\odot}$ yr^{-1}]	∼900	∼600
Detected Emission Lines		
$I_{CO(6-5)}$ [Jy km s^{-1}]	1.17 ± 0.27	0.77 ± 0.20
$I_{CO(9-8)}$ [Jy km s^{-1}]	0.93 ± 0.14	0.62 ± 0.18
$I_{CO(11-10)}$ [Jy km s^{-1}]	1.24 ± 0.21	0.65 ± 0.17
$I_{CO(13-12)}$ [Jy km s^{-1}]	1.24 ± 0.37	…
$I_{CO(14-13)}$ [Jy km s^{-1}]	0.67 ± 0.24	…
$I_{H_2O(3_{12}-3_{03})}$ [Jy km s^{-1}]	0.42 ± 0.09	0.47 ± 0.12
$I_{H_2O(4_{22}-4_{13})}$ [Jy km s^{-1}]	0.50 ± 0.17	…
$I_{H_2O(2_{02}-1_{11})}$ [Jy km s^{-1}]	0.45 ± 0.12	…
$FWHM_{CO(6-5)}$ [km s^{-1}]	440 ± 75	417 ± 86
$FWHM_{CO(9-8)}$ [km s^{-1}]	411 ± 53	533 ± 61
$FWHM_{CO(11-10)}$ [km s^{-1}]	658 ± 162	489 ± 141
$FWHM_{CO(13-12)}$ [km s^{-1}]	508 ± 121	…
$FWHM_{CO(14-13)}$ [km s^{-1}]	518 ± 97	…
$FWHM_{H_2O(3_{12}-3_{03})}$ [km s^{-1}]	444 ± 87	631 ± 92
$FWHM_{H_2O(4_{22}-4_{13})}$ [km s^{-1}]	852 ± 192	…
$FWHM_{H_2O(2_{02}-1_{11})}$ [km s^{-1}]	679 ± 174	…

460 μm flux density of A–1 and A–2. It can be seen that the observed FIR SEDs of A–1 and A–2 are fainter at mm wavelengths at a fixed FIR flux density than Arp 220 and ALESS, suggesting that A–1 and A–2 are warmer than the average SMG, although their dust temperatures are still comparable with the spread of the $T_{dust} - L_{IR}$ relation reported in Swinbank et al. (2014). At the IR luminosity of A–1, the mean dust temperature of SMGs is $T_{dust} \sim 34 \pm 8$ K, and at the IR luminosity of A–2 is $T_{dust} \sim 33 \pm 7$ K, where the uncertainties indicate the standard deviations.

4. Dust Morphology on 150 pc Scales

We focus this section on the analysis of the dust continuum emission detected in B7 (∼920 μm) and B6 (∼1.23 mm) in our two dusty starbursts. We first discuss the dust emission at ∼920 μm, and then we focus on the emission at ∼1.23 mm. A–1, the most luminous component of the pair (Figure 4 left), is resolved into three star-forming clumps, A–1A, A–1B, and A–1C, with A–1A being more than twice brighter than the other two components. Two star-forming clumps (A–2A and A–2B) are detected in A–2. We have measured the primary-beam corrected flux density at 920 μm and beam-deconvolved size of each component with the task IMFIT within CASA. The derived values are quoted in Table 2, where we only include the two clumps that are detected at $>10\sigma$ (A–1A and A–2A), since

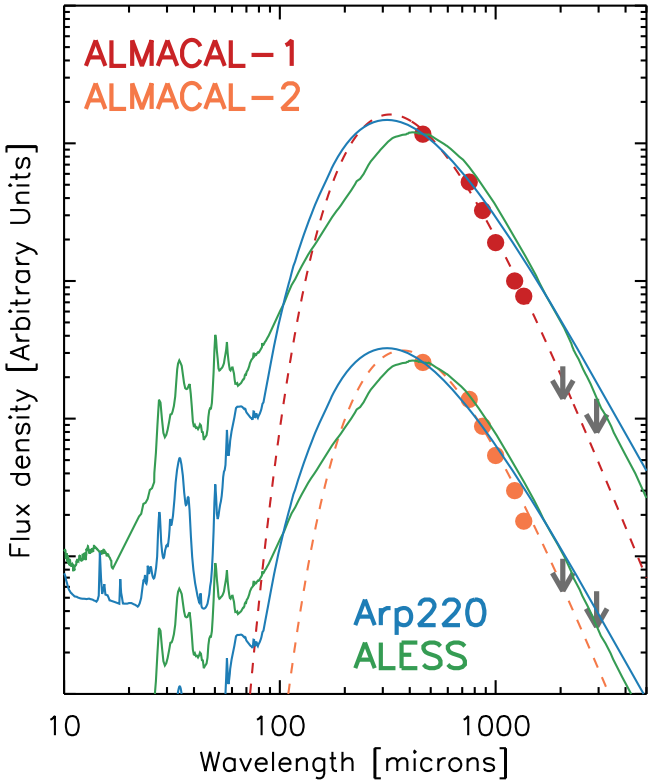

Figure 3. FIR SED of A–1 (red) and A–2 (orange). All photometric points come from the multiband observations in ALMA bands 6, 7, 8, and 9. Since there are available data on each side of B6 and B7, we have split the data for those bands in two subbands. With this, we have six photometric points for each source (and two 5σ upper limits in ALMA bands 4 and 3, indicated by the gray arrows). It should be noted that the error bars on the photometric points are smaller than the size of the filled dots. The FIR SEDs have been fitted assuming optically thin models with dust emissivity $\beta = 2.0$ (dashed curves) to derive their dust temperature, and total IR luminosities (see Table 1). For a reference, we have included the templates associated to the average FIR SED of ALESS SMGs (Swinbank et al. 2014) and Arp 220, redshifted to $z = 3.442$ and rescaled using the observed 460 μm flux density of each source.

sizes cannot be reliably measured at lower S/N (Simpson et al. 2015). We see that components A–1A and A–2A dominate the dust emission in A–1 and A–2, respectively, and appear very compact, with FWHM sizes of ∼300 pc.

Figure 4 also shows the ultrahigh spatial resolution 1.23 mm emission in our pair of submillimeter sources. At $z = 3.442$, this wavelength probes the emission at rest-frame ∼280 μm. The spatial resolution of the B6 observations (29 mas × 25 mas) is slightly worse than the resolution of the 920 μm observations, but still comparable. The maximum of the 1.23 mm emission is coincident with the maximum of the 920 μm emission. The lack of detected emission at 1.23 mm in components A–1B, A–1C, and A–2B is compatible with the fact that the r.m.s of the B6 observations is higher than in B7, that dusty starbursts are fainter in B6 than in B7 (see Figure 3 and Table 1), and that dust temperature variations can occur, so that components that are undetected at 1.23 mm can be associated with warmer dust temperatures. There seems to be an elongation of the 1.23 mm emission in A–1A that is not seen in the 920 μm map. The origin of this extended emission is currently unknown, although further data on this source providing higher S/N detections or better uv coverage will help to explore this issue further. We also note that, as pointed out in Hodge et al. (2016), caution has to be taken when analyzing faint signatures at high-spatial resolution.

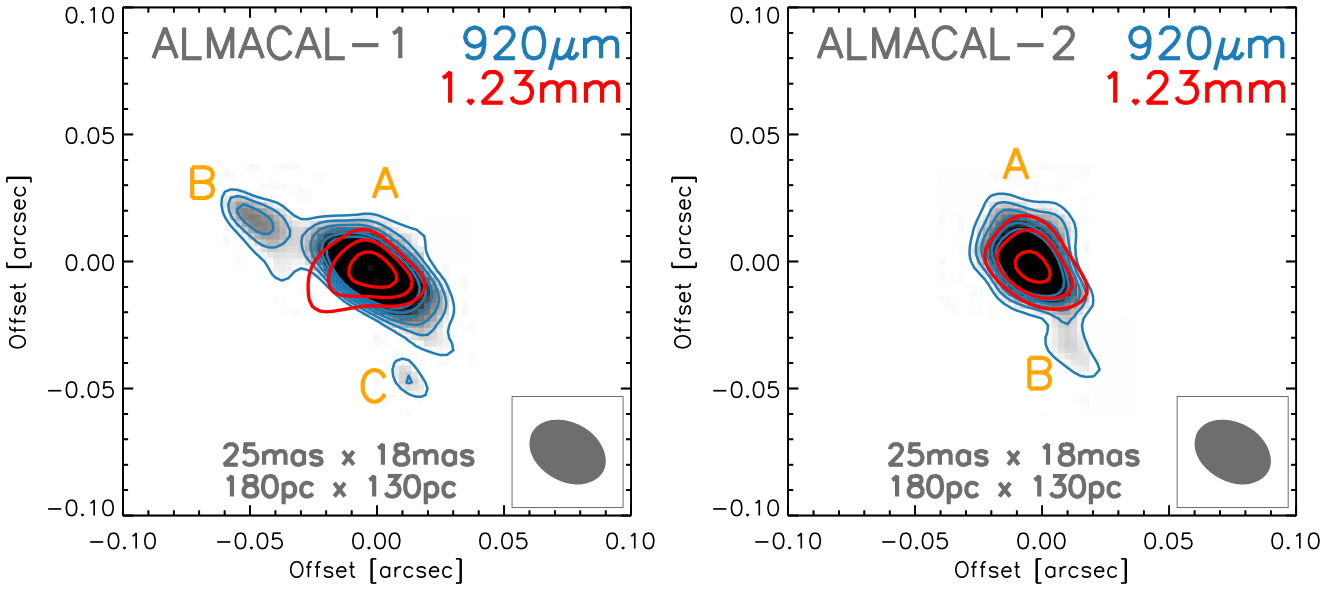

Figure 4. Ultrahigh-resolution imaging of ALMACAL–1 (A–1: left) and ALMACAL–2 (A–2: right). The background images and blue contours represent the 920 μm emission, while red contours are 1.2 mm emission. The synthesized beam and its size, both in sky and physical units, are indicated on each panel. All contours are represented from 5σ, in steps of 1σ. It should be noted that the spatial resolution of our observations is about 10× times better than previous observations of high-redshift unlensed starbursts, and it is only comparable with the source-plane resolution of the ALMA long-baseline observations of SDP.81 (ALMA Partnership et al. 2015) and the Eyelash (Swinbank et al. 2010). The dust emission in A–1 (left) is resolved into three different star-forming clumps (A–1A, A–1B, A–1C), while A–2 is resolved into two clumps (A–2A and A–2B). The flux densities of each clump in combination with their sizes reveal SFR surface densities significantly higher than those reported so far in high-redshift starbursts. Note that the size of each image is only 0.″2 on each side.

In any case, the similarity between the B6 and B7 emission in A–1A and A–2A confirms that the dust emission in these two components is truly compact. Using the best-fit FIR SEDs of A–1 and A–2 (see Figure 3), we estimate that their flux densities at 920 μm are $S_{920\,\mu\mathrm{m}} = 5.3 \pm 0.2$ mJy and $S_{920\,\mu\mathrm{m}} = 3.5 \pm 0.2$ mJy, respectively. Considering the observed flux densities in our ultrahigh-resolution data (see Table 2), we estimate that we resolve out about 40% of the observed flux in A–1 and A–2. This suggests that a significant fraction of the dust emission in our two dusty starbursts is relatively diffuse and/or extended, but that ∼60% of the dust emission in A–1 and A–2 is extremely compact.

The total IR luminosity of each clump has been obtained by rescaling the best-fit mid-IR power law plus the optically thin dust emission to A–1 and A–2 to their observed 920 μm flux density. The uncertainties of the total IR luminosities are the same for all clumps and reflect the errors in the extrapolation from a single-band photometry to the total IR luminosity (changes in dust temperature, dust emissivity, power law of the mid-IR SED, etc.). The associated SFRs have been derived using the classical Kennicutt (1998) calibration and assuming a Salpeter IMF. The SFR of our star-forming clumps ranges from ∼80 to ∼330 $M_\odot$ yr^{-1}. It is notable that the high SFR in A–1A and A–2A is taking place in extremely small star-forming clumps, with average FWHM sizes of about 300 pc. This means that the SFR surface density, Σ_{SFR}, of the clumps is as high as $\Sigma_{\mathrm{SFR}} \sim 3000\,M_\odot\,\mathrm{yr}^{-1}\,\mathrm{kpc}^{-2}$ (see Table 2). High values of the SFR surface densities like this have not been reported so far in any high-redshift dust starburst, and they exceed the maximum value predicted by Andrews & Thompson (2011), $\sim 1000\,M_\odot\,\mathrm{yr}^{-1}\,\mathrm{kpc}^{-2}$. It should be noted that SFR surface density values obtained for our sources would be still higher than the maximum value predicted by Andrews & Thompson (2011) when using the updated SFR calibrations by Kennicutt & Evans (2012).

Simpson et al. (2015) reported a median value of $90 \pm 30\,M_\odot\,\mathrm{yr}^{-1}\,\mathrm{kpc}^{-2}$ for their SMGs, with only two galaxies above $500\,M_\odot\,\mathrm{yr}^{-1}\,\mathrm{kpc}^{-2}$. In SGP 38326, the most luminous unlensed starburst found at $z > 4$, the star formation is taking place in two interacting disks, with the SFR density of the most luminous component of the merger being $\sim 840\,M_\odot\,\mathrm{yr}^{-1}\,\mathrm{kpc}^{-2}$ (Oteo et al. 2016a). For the Eyelash, a strongly lensed starburst at $z \sim 2.3$ whose star formation is occurring in four distinct clumps (FWHM $\sim 100 - 300$ pc), Thomson et al. (2015) derived values as high as $\Sigma_{\mathrm{SFR}} \sim 1650\,M_\odot\,\mathrm{yr}^{-1}\,\mathrm{kpc}^{-2}$. Other extreme dusty starbursts at high redshift have high SFR surface densities, such as HFLS3 ($\sim 600\,M_\odot\,\mathrm{yr}^{-1}\,\mathrm{kpc}^{-2}$) or AzTEC-3 ($\sim 850\,M_\odot\,\mathrm{yr}^{-1}\,\mathrm{kpc}^{-2}$), but none of them are comparable to the values found in A–1 and A–2. Relatively low values of the SFR surface density are also found in extreme high-redshift galaxies, such as HDF 850.1, with $\Sigma_{\mathrm{SFR}} \sim 35\,M_\odot\,\mathrm{yr}^{-1}\,\mathrm{kpc}^{-2}$. It is clear that there is a significant variety of Σ_{SFR} values in high-redshift galaxies. This could be because most previous observations did not have the spatial resolution to resolve the most compact emission (see also the discussion below).

The reason that all previous Σ_{SFR} at high redshift was significantly lower than in the star-forming clumps of A–1 and A–2 is likely a combination of their brightness and the availability of ultrahigh spatial resolution observations, which reveal that the strong star formation is occurring on very small scales (see also Iono et al. 2016). Most previous work on unlensed SMGs employed observations with a linear resolution around 10× times lower than the resolution of our ALMA data. To highlight the importance of ultrahigh spatial resolution observations in the analysis of the ISM of dusty starbursts, we have determined the size of the dust emission and the derived value of Σ_{SFR} in A–1 and A–2 by using our medium-resolution observations (see Figure 1 and Section 2). The smaller beam is provided by the B9 observations, 0.″50 × 0.″30. With this, A–1 has a beam-deconvolved size of 345 mas × 194 mas, or 2.5 kpc × 1.4 kpc.

Table 2
Observed Properties of the Star-forming Clumps Found in A–1 and A–2

Clump	$S_{920\,\mu m}$ (mJy)	$\log(L_{IR}/L_\odot)$[a]	SFR ($M_\odot$ yr^{-1})	A_d[b] (mas × mas)	A_d[b] (pc × pc)	Σ_{IR}[c] ($L_\odot$ kpc^{-2})	Σ_{SFR} ($M_\odot$ yr^{-1} kpc^{-2})	S/N
A–1A	2.0 ± 0.1	12.2 ± 0.2	∼310	49 ± 5 × 25 ± 3	360 ± 40 × 180 ± 20	∼1.7 × 10^{13}	∼3015	19.1
A–1B	0.9 ± 0.1	11.9 ± 0.2	∼140	⋯	⋯	⋯	⋯	8.3
A–1C	0.5 ± 0.1	11.6 ± 0.2	∼80	⋯	⋯	⋯	⋯	6.5
A–2A	2.1 ± 0.2	12.3 ± 0.2	∼330	57 ± 5 × 34 ± 4	420 ± 40 × 250 ± 30	∼1.2 × 10^{13}	∼2035	15.5
A–2B	0.8 ± 0.1	11.8 ± 0.2	∼110	⋯	⋯	⋯	⋯	5.9

Notes.
[a] The total IR luminosities have been calculated from the observed flux density at 920 μm assuming the best-fit FIR SEDs obtained from the medium-resolution data (see Figure 3). Furthermore, we assume that all IR luminosity is due to star formation rather than AGN activity.
[b] The sizes reported in the table correspond to the beam-deconvolved FWHM of a 2D elliptical Gaussian fit. We only report the size of the clumps detected at S/N >10. Size of ALMA-detected sources at lower S/N are not reliable (Simpson et al. 2015).
[c] The surface densities have been calculated assuming that the size of the sources is $\pi R_a \times R_b$, where R_a and R_b are the semi-axis of the best-fit elliptical Gaussian of each component. Furthermore, we have divided the SFR of each component by a factor of two because their size corresponds to the half-light radius.

This would imply $\Sigma_{SFR} \sim 165\,M_\odot$ yr^{-1} kpc^{-2}, compatible with the values found by Simpson et al. (2015), but more than one order of magnitude lower than the Σ_{SFR} of any of the three components A–1 is resolved into when observed at ultrahigh spatial resolution.

Wilson et al. (2014) reported high-resolution observations of the two nuclei of Arp 220 at ∼0.″3 × 0.″2. In physical scale, their spatial resolution (∼130 pc × 70 pc) matches our ultrahigh spatial resolution. Wilson et al. (2014) obtained an IR surface density of $\Sigma_{IR} = 2.1 \times 10^{14}\,L_\odot$ kpc^{-2} and $\Sigma_{IR} = 5.8 \times 10^{12}\,L_\odot$ kpc^{-2} for the western and eastern nuclei, respectively. These values are similar to the values we find for A–1 and A–2 and were obtained at similar physical spatial resolution, highlighting again that ultrahigh spatial resolution plays a key role in the understanding the properties and nature of dusty starbursts.

It is possible that some of the observed L_{IR} in our two submillimeter sources might be due to dust heated by an AGN in the center of the galaxies instead of star formation. In fact, Wilson et al. (2014) discussed that the extremely high luminosity surface densities found in the western nucleus of Arp 220 could in part be due to the presence of an AGN. If there is AGN contribution to the luminosity of the brightest clumps in A–1 and A–2, their SFRs would be overestimated, and so would the associated SFR surface densities. It could be expected that if there is AGN contribution in our two submillimeter sources, the AGN is located in the two brightest clumps, but not in the fainter ones. Even if the SFR surface density of the brightest clumps might be overestimated, this is therefore less likely to happen in the fainter clumps, and these still have high SFR surface densities. This assumes that the possible AGN heat the dust locally over a scale of less than 200 pc, which does not reachi the other star-forming clumps.

4.1. Potential Lensing

As noted in Section 3, the fact that the flux ratio (both line and continuum) between A–1 and A–2 appears to vary with wavelength suggests that these sources are not two gravitationally amplified images of a single galaxy at $z = 3.442$ close to the line of sight of the blazar host. Nevertheless, in order to investigate what the consequences of lensing would be, we consider in this section the possibility that A–1/A–2 is actually a lensed system. If this is the case, we need to calculate the flux and size of the source in the source plane. To do this we have used the code `uvmcmcfit`, which models the lensed emission of galaxies observed with interferometers in the *uv* plane (Bussmann et al. 2013, 2015). In `uvmcmcfit` the background source is assumed to have an elliptical Gaussian profile characterized by six free parameters: the position of the source, the total intrinsic flux density, the effective radius length, the axial ratio, and the position angle. The lens mass profile is represented by a singular isothermal ellipsoid with five parameters: the position of the lens, the Einstein radius, the axial ratio of the lens, and its position angle. We have assumed that the lens (the blazar host) is coincident with the calibrator continuum emission, excluding the jet (red cross in Figure 1).

We first modeled the possible lensed emission in the medium-resolution maps (see Figure 1) with the aim of exploring whether the spatial configuration of A–1 and A–2 with respect to the lens can be reproduced successfully. We modeled the lensed emission in all bands where A–1 and A–2 are detected (see Table 1). The result is that the positions and flux ratios of the two sources are well reproduced in all bands. It should be noted that we did not model the multiband emission simultaneously since this is not possible to do with publicly available codes working in the *uv* plane. The magnification factor is derived from the ratio between the total flux density in the lensed image of the model to the total flux density in the unlensed intrinsic source model. We derived $\mu_{dust} = 7.4 \pm 0.1$ at 870 μm from the combined flux from A–1 and A–2, and similar values are obtained in the other bands (which is expected because of the similar spatial configuration of the system in the different bands). The Einstein radius is $\theta_E = 1.83 \pm 0.01$, the ellipticity of the lens $\epsilon_L = 0.81 \pm 0.02$, and the source is located 0.″44 north and 0.″40 west of the lens. With these numbers, the effective radius of the source in the source plane is $R_{eff} \sim 340$ pc. We then used the best-fit model obtained from the medium-resolution data as an initial condition to model the possible lensed emission in the ultrahigh-resolution observations. If they are lensed, the observed emission in A–1 and A–2 (see Figure 4) is compatible with a single extremely compact background source, whose effective radius is only $R_{eff} \sim 40$ pc.

The total observed SFR of A–1 and A–2 in the ultrahigh-resolution observations is SFR ∼ 870 $M_\odot$ yr^{-1}, which corresponds to a source-plane demagnified SFR of ∼120 $M_\odot$ yr^{-1}. Together with the effective radius in the source plane, the demagnified SFR surface density is Σ_{SFR} ∼10,000 $M_\odot$ yr^{-1} kpc^{-2}. This value is considerably higher than the

values obtained considering that A–1 and A–2 are not lensed and is therefore much higher than in any previous high-redshift source and very close to the value found in the eastern nucleus of Arp 220.

5. Conclusions

In this paper we have presented ultrahigh spatial resolution (∼20 mas) dust continuum (870 μm and 1.2 mm) observations of two dusty starbursts, the brightest submillimeter sources detected so far in our survey of serendipitous sources in the fields of ALMA calibrators: A–1 ($S_{870\,\mu\mathrm{m}} = 6.5 \pm 0.2$ mJy) and A–2 ($S_{870\,\mu\mathrm{m}} = 4.4 \pm 0.2$ mJy). The main conclusions of our work are the following:

1. We have determined the spectroscopic redshift of our two dusty starbursts to be $z = 3.442$ via detection of up to nine ^{12}CO and H_2O emission lines in ALMA bands 4, 6, and 7. The maximum velocity shift found between the emission lines of A–1 and A–2 (which are separated on the sky by 28 kpc) is less than 100 km s^{-1}, significantly lower than in other high-redshift interacting starbursts.
2. Using flux densities measured in ALMA band 6, 7, 8, and 9, we have determined the dust temperature and total IR luminosity of each of the two dusty starbursts. These values are compatible with those found for the classical population of SMGs (with A–1 being warmer than A–2), and they would have been selected as SMGs in single-dish submillimeter surveys. Uniquely, the FIR SEDs of our two dusty starbursts have been constrained with subarcsecond resolution observations, unlike in previous work, which was based on single-dish FIR/submillimeter observations, which suffer from large beam sizes and source confusion problems.
3. Our ALMA ultrahigh-resolution imaging reveals that about half of the dust emission in A–1 and A–2 is arising in compact components (with FWHM sizes of ∼350 pc). Two additional fainter star-forming clumps are found in A–1. We recall that our in-field calibrator and subsequent self-calibration ensures near-perfect phase stability on the longest baselines, ensuring great image quality. We have two independent data sets in ALMA B6 and B7 at similar spatial resolution that prove the reliability of the reported structures.
4. The high SFR and the compact size of all the star-forming clumps in A–1 and A–2 indicate extremely high SFR surface densities of up to $\Sigma_{\mathrm{SFR}} \sim 6000\,M_\odot\,\mathrm{yr}^{-1}\,\mathrm{kpc}^{-2}$. These values are significantly higher than those previously obtained in high-redshift dusty starbursts and are only comparable to the values found in the nuclei of Arp 220 with observations at similar (physical) spatial resolution. It should be noted that the SFR is obtained assuming that the IR luminosity is due to star formation, since with the current data we cannot study the contribution of a possible AGN to the SFR.
5. We argue that the extremely high SFR surface densities of the star-forming clumps in A–1 and A–2 might be common in high-redshift dusty starbursts, but that they are only visible thanks to the availability of ultrahigh spatial resolution data. This highlights the importance of long-baseline observations for the study of the ISM of dusty starbursts in the early Universe.
6. There is a possibility that this system is lensed, in the sense that the two submillimeter sources around J1058 +0133 are the lensed emission of a source that is gravitationally amplified by the blazar host. If this were the case, the resolution of the observations would increase to ∼50 pc and we would be resolving sizes comparable to individual giant molecular clouds. The galaxy in the source plane would have an effective radius of $R_{\mathrm{eff}} \sim 40$ pc, implying a demagnified SFR surface density of $\Sigma_{\mathrm{SFR}} \sim 10{,}000\,M_\odot\,\mathrm{yr}^{-1}\,\mathrm{kpc}^{-2}$, which is only comparable with the value found in the eastern nucleus of Arp 220.

I.O. and R.J.I. acknowledge support from the European Research Council in the form of the Advanced Investigator Programme, 321302, COSMICISM. We acknowledge stimulating discussions with Zhi-Yu Zhang and Mathilde Jauzac for her help and for providing an initial lens model. I.R.S. acknowledges support from STFC (ST/L00075X/1), the ERC Advanced Investigator programme DUSTYGAL 321334 and a Royal Society/Wolfson Merit Award. This paper makes use of the following ALMA data: ADS/JAO.ALMA#2015.1.01518.S, ADS/JAO.ALMA#2015.1.00695.S, ADS/JAO.ALMA#2015.1.00686.S, ADS/JAO.ALMA#2015.1.01302.S, ADS/JAO.ALMA#2015.1.01345.S, ADS/JAO.ALMA#2015.1.00607.S, ADS/JAO.ALMA#2015.1.00597.S, ADS/JAO.ALMA#2015.1.00928.S, ADS/JAO.ALMA#2015.1.00665.S. ALMA is a partnership of ESO (representing its member states), NSF (USA) and NINS (Japan), together with NRC (Canada) and NSC and ASIAA (Taiwan) and KASI (Republic of Korea), in cooperation with the Republic of Chile. The Joint ALMA Observatory is operated by ESO, AUI/NRAO and NAOJ.

References

ALMA Partnership et al. 2015, ApJL, 808, L4
Andrews, B. H., & Thompson, T. A. 2011, ApJ, 727, 97
Asboth, V., Conley, A., Sayers, J., et al. 2016, MNRAS, 462, 1989
Barger, A. J., Cowie, L. L., Chen, C.-C., et al. 2014, ApJ, 784, 9
Barger, A. J., Cowie, L. L., Sanders, D. B., et al. 1998, Natur, 394, 248
Blain, A. W., Smail, I., Ivison, R. J., Kneib, J.-P., & Frayer, D. T. 2002, PhR, 369, 111
Bussmann, R. S., Pérez-Fournon, I., Amber, S., et al. 2013, ApJ, 779, 25
Bussmann, R. S., Riechers, D., Fialkov, A., et al. 2015, ApJ, 812, 43
Casey, C. M. 2012, MNRAS, 425, 3094
Chapman, S. C., Blain, A. W., Smail, I., & Ivison, R. J. 2005, ApJ, 622, 772
Dye, S., Negrello, M., Hopwood, R., et al. 2014, MNRAS, 440, 2013
Dye, S., Furlanetto, C., Swinbank, A. M., et al. 2015, MNRAS, 452, 2258
Eales, S., Dunne, L., Clements, D., et al. 2010, PASP, 122, 499
Engel, H., Tacconi, L. J., Davies, R. I., et al. 2010, ApJ, 724, 233
Frayer, D. T., Harris, A. I., Baker, A. J., et al. 2011, ApJL, 726, L22
Hodge, J. A., Karim, A., Smail, I., et al. 2013, ApJ, 768, 91
Hodge, J. A., Swinbank, A. M., Simpson, J. M., et al. 2016, ApJ, 833, 103
Hughes, D. H., Serjeant, S., Dunlop, J., et al. 1998, Natur, 394, 241
Ikarashi, S., Ivison, R. J., Caputi, K. I., et al. 2015, ApJ, 810, 133
Iono, D., Yun, M. S., Aretxaga, I., et al. 2016, ApJL, 829, L10
Ivison, R. J., Greve, T. R., Dunlop, J. S., et al. 2007, MNRAS, 380, 199
Ivison, R. J., Swinbank, A. M., Smail, I., et al. 2013, ApJ, 772, 137
Karim, A., Swinbank, A. M., Hodge, J. A., et al. 2013, MNRAS, 432, 2
Kennicutt, R. C. Jr. 1998, ARA&A, 36, 189
Kennicutt, R. C., & Evans, N. J. 2012, ARA&A, 50, 531
Magnelli, B., Lutz, D., Santini, P., et al. 2012, A&A, 539, A155
Negrello, M., Hopwood, R., De Zotti, G., et al. 2010, Sci, 330, 800
Negrello, M., Hopwood, R., Dye, S., et al. 2014, MNRAS, 440, 1999
Oteo, I., Zwaan, M. A., Ivison, R. J., Smail, I., & Biggs, A. D. 2016b, ApJ, 822, 36
Oteo, I., Ivison, R. J., Dunne, L., et al. 2016a, ApJ, 827, 34

Rybak, M., McKean, J. P., Vegetti, S., Andreani, P., & White, S. D. M. 2015a, MNRAS, 451, L40
Rybak, M., Vegetti, S., McKean, J. P., Andreani, P., & White, S. D. M. 2015b, MNRAS, 453, L26
Salpeter, E. E. 1955, ApJ, 121, 161
Simpson, J. M., Swinbank, A. M., Smail, I., et al. 2014, ApJ, 788, 125
Simpson, J. M., Smail, I., Swinbank, A. M., et al. 2015, ApJ, 799, 81
Smail, I., Ivison, R. J., & Blain, A. W. 1997, ApJL, 490, L5
Strandet, M. L., Weiss, A., Vieira, J. D., et al. 2016, ApJ, 822, 80
Swinbank, A. M., Smail, I., Longmore, S., et al. 2010, Natur, 464, 733
Swinbank, A. M., Simpson, J. M., Smail, I., et al. 2014, MNRAS, 438, 1267
Swinbank, A. M., Dye, S., Nightingale, J. W., et al. 2015, ApJL, 806, L17
Tacconi, L. J., Genzel, R., Smail, I., et al. 2008, ApJ, 680, 246
Thomson, A. P., Ivison, R. J., Owen, F. N., et al. 2015, MNRAS, 448, 1874
Wang, W.-H., Cowie, L. L., Barger, A. J., & Williams, J. P. 2011, ApJL, 726, L18
Weiß, A., Ivison, R. J., Downes, D., et al. 2009, ApJL, 705, L45
Weiß, A., De Breuck, C., Marrone, D. P., et al. 2013, ApJ, 767, 88
Wilson, C. D., Rangwala, N., Glenn, J., et al. 2014, ApJL, 789, L36